Asymmetric Mode Control of MMC to Suppress Capacitor Voltage Ripples in Low-Frequency, Low-Voltage Conditions

Rongfeng Yang, Binbin Li, *Student Member, IEEE*, Gaolin Wang, *Member, IEEE*, Carlo Cecati, *Life Fellow, IEEE*, Shaoze Zhou, Dianguo Xu, *Senior Member, IEEE*, and Wanneng Yu

***Abstract*—This paper proposes an asymmetric mode control for a modular multilevel converter (MMC) operating at low-frequency and low-output-voltage conditions. Differently from conventional symmetric operations, affected by large capacitor voltage ripples caused by the large dc-link voltage, with the proposed asymmetric mode MMC operations, one arm does not produce output current and applies the major dc-link voltage, whereas the other arm sustains almost all output current with low dc-link voltage. Variations of the power level in arms remain bounded and the MMC does not need any other power exchange technique such as high-frequency or harmonic current injection in a low-frequency/low-voltage condition to suppress the capacitor voltage ripple. The asymmetric control realization, and arm energy regulation and its optimization are presented in detail. Experimental and simulation results show that the proposed method is suitable for motor drives operating under 20 Hz.**

***Index Terms*—Capacitor voltage fluctuation/ripple, energy balance, harmonics injection, modular multilevel converter (MMC), motor drives.**

I. Introduction

BECAUSE of their scalability, flexibility, and controllability, modular multilevel converters (MMC), as shown in Fig. 1, are attracting significant interest for numerous high-power applications [1]–[3], such as high-voltage direct current transmission [4]–[7], high-voltage dc/dc transformers [8]–[10], grid-connected inverters [11], [12], and medium-voltage motor drives [13], [14]. In fact, due to their staircase-like output, approximating sinusoidal waveforms much better than conventional two-level converters, the large number of series/parallel-connected submodules (SMs) with a relatively low-voltage rating produce a high voltage keeping low-output harmonics. In particular, MMC drives due to their excellent quality of output voltage and current, reduced torque ripples, and motor harmonic losses [13], meeting the requirements of medium-voltage motors, are becoming a structure of interest for such kinds of application.

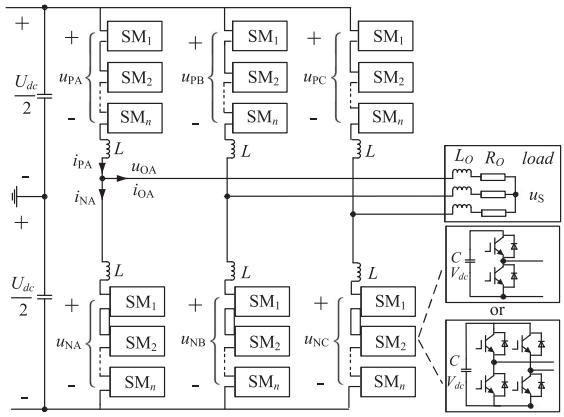

Fig. 1. Modular multilevel converter.

An important issue in MMCs for motor drives is that they usually operate in a relatively large frequency range, including very low frequencies. The resulting voltage ripple measurable at the terminal of each MMC chopper cell floating capacitor, being proportional to the motor current and inversely proportional to the motor frequency, could not be tolerated, particularly at low speed [14]. This is one of the intrinsic drawbacks of MMCs and it depends on the lack of power exchange or sharing among arms. Previous research works suggested the use of MMC inverters only in drives with low dynamics operating at high speed (fans, compressors, pumps, etc.), i.e., those with a small torque at low speed. This challenge triggers researchers to propose new techniques to deal with this problem.

According to the current literature, the methods for reducing capacitor ripples can be classified into two distinct categories. The first one consists of injecting specific harmonics within the circulating current [15]–[17]. The relationship between circulating current harmonics and capacitor voltage is analyzed in

Manuscript received February 25, 2016; revised May 12, 2016 and July 18, 2016; accepted August 2, 2016. Date of publication August 16, 2016; date of current version February 11, 2017. This work was supported by the Qianren Talents Plan of China, by the National Nature Science Foundation of China under Grants 51237002 and 51477034, by the project from the Ministry of Transport of the People's Republic of China under Grant 201507160002. Recommended for publication by Associate Editor M. Hagiwara.

R. Yang and W. Yu are with the School of Marine Engineering, Jimei University, Xiamen, China (e-mail: yrf.hit@gmail.com; ywn_post1@126.com).

B. Li, G. Wang, S. Zhou, and D. Xu are with the School of Electrical Engineering and Automation, Harbin Institute of Technology, Harbin, China (e-mail: libinbinhit@126.com; wgl818@hit.edu.cn; 1378392610@qq.com; xudiang@hit.edu.cn).

C. Cecati is with the Electrotechnical Engineering from the University of LÁquila, LÁquila, Italy (e-mail: carlo.cecati@digipower.it).

Color versions of one or more of the figures in this paper are available online at http://ieeexplore.ieee.org.

Digital Object Identifier 10.1109/TPEL.2016.2600762

[15], in which a second harmonic signal is injected for capacitor ripple reduction. Similar work was carried out in [16] considering the fourth harmonic. The third harmonic common mode voltage is also utilized to maximize the modulation range [17]. These methods can attenuate ripples caused by converter output voltage and current (second order) effectively. But, unfortunately, capacitor voltage ripples at low motor speed operations are mainly caused by dc-link voltage and output current at a fundamental frequency. Thus, this method has significant limitations in motor drive applications.

Another strategy is to inject a high-frequency signal in circulating currents while injecting the same frequency harmonic to the converter output common mode voltage [18]–[21]. The injected harmonics will generate positive or negative power, thus achieving energy balancing for arms. The common mode voltage will not change the line-to-line voltage in motor control; thus, it has no influence on the motor drive voltage. Some square waveforms [18] or other optimized currents [19] can also be injected instead of sinusoids, thus enhancing the compensation effect. This method can ensure full motor speed range control after optimization [13], but the control of high-frequency harmonics is complex, as it is necessary to comprehensively consider a tradeoff between modulation range, loss, and capacitor ripple magnitude.

Some other researchers proposed modifications for MMC, e.g., [22]–[24], or a new topology [25], [26], but full speed range capability even at a constant torque load and cost reduction need further research.

The contributions of this paper are as follows:

1) analyze the conventional control with the relative capacitor ripple, showing that the symmetric operation mode of conventional MMC control generates significant capacitor ripples, thus making energy balance control between upper and lower arms difficult;
2) propose a new asymmetric operation control strategy to avoid the dc-link voltage influence on capacitor ripples;
3) show that with the proposed optimized alternating energy regulation control, arm energy can be individually controlled without coupling.

It should be pointed out that the "asymmetric control" concept has been mentioned in [27], and further investigated in [28], in which the arm currents are asymmetric; however, in [28], control is based on the discontinuous modulation technique, that is, one arm needs to be bypassed or clamped, which is different from the proposed method, which, in turn, is based on combined effects of a circulating current reference design, energy regulation, and alternating control.

The outline of this paper is as follows. The analysis of conventional symmetric control and its drawbacks are presented in Section II. The novel asymmetric operation mode concept is introduced in Section III-A. Following, the proposed control for asymmetric mode realization, energy regulation, and alternation control is described in Section III-B. Experimental results and verification of the proposed method are given in Section IV. Further study for limitations and optimization are discussed in Section V. Finally, some conclusions are summarized in Section VI.

II. Conventional Control and Capacitor Ripple Analysis

A. MMC Conventional Control

In Fig. 1, it can be seen that, for each phase, upper and lower arms can be considered equivalent to a voltage source converter (VSC), whose output is the sum of all the SM voltages. The voltages of the upper arm and lower arm are u_{Pi} and u_{Ni}, and the currents flowing through these two arms are i_{pi} and i_{Ni}, respectively, where $i = A, B,$ or C. From Kirchhoff's voltage law (KVL), it follows that

$$\frac{U_{\mathrm{dc}}}{2} = u_{\mathrm{Pi}} + L\frac{di_{\mathrm{Pi}}}{dt} + (u_{\mathrm{oi}} + u_{\mathrm{SG}}) \tag{1}$$

$$-\frac{U_{\mathrm{dc}}}{2} = -u_{\mathrm{Ni}} - L\frac{di_{\mathrm{Ni}}}{dt} + (u_{\mathrm{oi}} + u_{\mathrm{SG}}) \tag{2}$$

where u_{oi} is the voltage imposed on load (L_O and R_O) and is given by

$$u_{\mathrm{oi}} = L_O\frac{di_{\mathrm{Oi}}}{dt} + R_O i_{\mathrm{Oi}}. \tag{3}$$

As mentioned above, $i = A, B, C$, and it will be omitted later for simplification as all three phases have equivalent expressions. Assuming the voltage u_{SG} to be null (the voltage between the star point and the reference point *G*) at the motor-star terminal, which is reasonable in conventional control, which does not change the converter output zero-sequence voltage, the common mode and differential mode voltages can be deduced as

$$u_{\mathrm{comm}} = \frac{u_P + u_N}{2} = \frac{U_{\mathrm{dc}}}{2} - L\frac{d\left(\frac{i_p + i_N}{2}\right)}{dt} \tag{4}$$

$$u_{\mathrm{diff}} = (u_P - u_N) = -2u_o - L\frac{d(i_P - i_N)}{dt}. \tag{5}$$

Similarly, according to Fig. 1, the common mode and differential mode currents can be defined as

$$i_{\mathrm{comm}} = \frac{i_P + i_N}{2} \tag{6}$$

$$i_{\mathrm{diff}} = i_P - i_N. \tag{7}$$

The common mode current is also called the circulating current, and the differential current is the converter output current [17]. These two currents are decoupled and can be controlled in (4) and (6) by regulating u_{comm} and u_{diff}. After u_{comm} and u_{diff} are obtained, the arms' output voltages can be determined, which are the references for modulation, as

$$u_{P,N} = u_{\mathrm{comm}} \pm \frac{u_{\mathrm{diff}}}{2}. \tag{8}$$

With this control, assuming symmetric branch parameters, the output current shall be equally split between arms [15]. From (1)–(8), it can be found that with conventional control, the quantities of both upper and lower arms are symmetric. This helps the two arms to achieve a maximum linear operation range for modulation, and share the output current to reduce ratings.

B. Branch power analysis

In practical application, u_o and i_o are imposed by load. Here, they are assumed to be sinusoidal in motor drives for simplification. Based on this assumption and neglecting the electromotive

force on inductor, from (4), (5) and (8), the arm voltages can be obtained as

$$u_{P,N} = \frac{U_{\rm dc}}{2} \mp u_O = \frac{U_{\rm dc}}{2} \mp U_O \sin(\omega t) \tag{9}$$

where, for the sake of brevity, the equation stands for u_P when the second right term is negative and for u_N when the terms are summed up. Assuming that the circulating current is $I_{\rm cir}$, which charges or discharges the SMs, keeping the arm energy equivalent. It is constant in steady state, but it can be adjusted to contain harmonics, if necessary. From (6) and (7), the arm current can be expressed as

$$i_{P,N} = I_{\rm cir} \pm \frac{i_O}{2} = I_{\rm cir} \pm \frac{I_O}{2} \sin(\omega t + \varphi). \tag{10}$$

From (9), the instantaneous power of the arms, which is relative to the capacitor voltage variation [14], is given by

$$\begin{aligned} P_{P,N} &= u_{P,N} \cdot i_{P,N} \\ &= \frac{U_{\rm dc} I_{\rm cir}}{2} - \frac{U_O I_O}{4} \cos\varphi + \frac{U_O I_O}{4} \cos(2\omega t + \varphi) \\ &\pm \left(\frac{U_{\rm dc} I_O}{4} \sin(\omega t + \varphi) - U_O I_{\rm cir} \sin(\omega t) \right). \end{aligned} \tag{11}$$

In (10), (11), and in the following equations, the sign "+" or "−" depends on "P" or "N". If voltage vs. frequency (V/f) control is applied, then we have

$$U_O = \frac{f_O U_m}{f_m} \tag{12}$$

where f_O is the converter voltage frequency and U_m is the maximum voltage imposed on the motor at the maximum frequency f_m, which is also half of the dc-link voltage in general design. It is worth noticing from (12) that U_O is small at low speed.

The first term in (11) is the power from the dc-link, which balances the load power or the second term. As the load power is small at low-frequency operation, $I_{\rm cir}$ maintains at a small level. Noting that $U_O \ll U_{\rm dc}$ at this time, the other terms can be ignored, except the fourth one. So, the power of the arms in a low-voltage condition can be presented as

$$P_{P,N} \approx \frac{U_{\rm dc} I_{\rm cir}}{2} - \frac{U_O I_O}{4} \cos\varphi \pm \frac{U_{\rm dc} I_O}{4} \sin(\omega t + \varphi). \tag{13}$$

It is remarkable that if the converter has a low output voltage, the third term contributes the most significant differential power between arms; moreover, due to the large values of $U_{\rm dc}$, its compensation could be difficult by using conventional symmetric control because both arms must be able to supply the necessary common components of $\frac{U_{\rm dc}}{2}$ and then the right amount of current $\frac{I_O}{2}$.

Another negative impact of symmetric control is that there is an interaction and a coupling between arms for energy control. For instance, if the upper arm needs to charge energy at one moment, then, from the third term of (13), the lower arm needs to discharge energy. But, the MMC structural feature with symmetric control determines that there are no measures to meet these two demands at the same time and the circulating current will charge or discharge these two arms simultaneously, as shown in the first term of (13). Finally, the energy imbalance causes an imbalance in arm capacitor voltages. This impact gets unsustainable and impractical at a low frequency, as the capacitor voltage depends on the integral of instantaneous power. Considering the condition in (13) and ignoring the first two terms because they must be kept equal in order to maintain energy equivalent between dc-link and load, the ac component of the upper arm capacitor voltage will be [14]

$$\begin{aligned} \widetilde{V}_{\rm dcP} &= \frac{1}{CV_{C0}} \int \widetilde{P}_P \, dt = \frac{1}{CV_{C0}} \int \frac{U_{\rm dc} I_O}{4} \sin(\omega t + \varphi) \, dt \\ &= -\frac{U_{\rm dc} I_O}{4CV_{C0}\omega} \cos(\omega t + \varphi) \end{aligned} \tag{14}$$

where V_{C0} denotes the dc component of the capacitor voltage. It is shown that the capacitor voltage ripple is inversely proportional to the frequency and the modules will face capacitor voltage overrating or overmodulation risks when MMC works at a low frequency.

In conclusion, conventional control ensures that the upper and lower arms share the power flow from dc-link to load, and the two arms can achieve a maximum linear operation range for modulation. However, this advantage is not relevant in low-frequency and low-voltage conditions. On the contrary, its drawbacks become remarkable at this condition in that the capacitor voltage ripple will exaggerate to a significant level by dc-link voltage and output current, which has a large amplitude and is hard to suppress.

III. Asymmetric Mode Operation

A. Asymmetric Mode Operation Analysis

In order to overcome previously discussed problems, this paper proposes a novel asymmetric mode operation. With this control, the arm voltages and currents have the forms

$$\begin{cases} u_P = -U_O \sin(\omega t) + K U_{\rm dc} \\ u_N = U_O \sin(\omega t) + (1-K) U_{\rm dc} \\ i_P = I_O \sin(\omega t + \varphi) \\ i_N = 0 \end{cases} \tag{15}$$

or the complementary ones

$$\begin{cases} u_P = U_O \sin(\omega t) + (1-K) U_{\rm dc} \\ u_N = -U_O \sin(\omega t) + K U_{\rm dc} \\ i_P = 0 \\ i_N = -I_O \sin(\omega t + \varphi). \end{cases} \tag{16}$$

The term $KU_{\rm dc}$, ensuring that both $u_P > 0$ and $u_N > 0$ are always verified, is very important for MMCs with half-bridge cells, whose arms can produce either zero or positive voltage; it is zero in the case of full bridges. Of course, $K = 1/2$ corresponds to the conventional symmetrical control. K is proportional to Uo according to

$$K = \frac{U_O}{U_{\rm dc}}. \tag{17}$$

Taking mode (15) as an example, the converter output voltage is

$$u_O = -\frac{u_P - u_N}{2} = U_O \sin(\omega t) - KU_{\rm dc} + \frac{U_{\rm dc}}{2}. \quad (18)$$

The last two terms are the zero-sequence (or common mode) voltage, which will not change the phase-to-phase voltage. It is also easy to verify that $u_P + u_N$ equals to $U_{\rm dc}$, thus meeting dc-link requirements.

The power of the upper and lower arms with the arm voltages and currents of (15) is

$$\begin{cases} P_P = -\frac{1}{2}U_O I_O \cos\varphi + \frac{1}{2}U_O I_O \cos(2\omega t + \varphi) \\ +KU_{\rm dc} I_O \sin(\omega t + \varphi) \\ P_N = 0 \end{cases}. \quad (19)$$

The first dc term in the upper arm power is the power supplied to the load and the other two terms are ac components. Since U_O is small, these terms have small magnitudes, being comparable with the load power. The lower arm sustains a major dc-link voltage, but the current being zero, there are no power fluctuations. Compared with the energy in (13), it can be seen that arm energy fluctuations keep ultralow. As energy fluctuations are significantly attenuated, the arm energy balance can be easily achieved. In addition, arm energy will be shared by all modules in this arm through the individual capacitor voltage balance technique [3].

However, there are still several issues to be solved to accomplish this control. On one hand, circulating current control should be deliberately designed to shape the voltage and current forms according to (15) and (16), while, on the other hand, the upper arm is continuously consuming energy (see Fig. 19), although in a small amount. So, this arm needs the charging process to maintain an energy level. In addition, as the charging process will cause the energy of the two arms to increase or decrease simultaneously, the upper and lower arms have to alternate their working mode, thus exchanging energy consuming and charging states. These are the control issues that will be addressed in the next section.

B. Asymmetric Operation Controller Design

This section deals with current and voltage regulation control, as well as arm energy charge control, necessary for effective asymmetric operation.

1) Asymmetric Mode Realization: There are two methods to realize asymmetric mode operation for MMC.

Method I: Comparing current waveforms of asymmetric mode (15) to symmetric mode (10), it can be found that the arm currents in (15) can be achieved only if the circulating current $I_{\rm cir}$ has the component $\frac{I_O}{2}\sin(\omega t + \varphi)$. Similarly, the arm currents for the complementary mode (16) can be achieved only if the circulating current has the component $-\frac{I_O}{2}\sin(\omega t + \varphi)$. So, the asymmetric mode can be realized by injecting one circulating current component that has half amplitude and the same (or opposite) phase angle as the converter output current.

Method II: As discussed above, in each phase, the output current in one arm is null, and there is only energy charging current $I_{\rm cir}$ left; thus, the asymmetric mode can be realized by directly driving this arm current to be $I_{\rm cir}$. The implementation is achieved by circulating current control, and the control diagram is provided in Section III-C.

2) Arm Alternating Operation: As discussed in the previous section, the arm generating the output current supplies energy to load and has to be charged to keep the capacitor voltage at a rating value. Considering that there is the charging current $I_{\rm cir}$ and the voltage $u_{\rm comm}$, which implement the circulating current control, (15) can be rewritten as

$$\begin{cases} u_P = -U_O \sin(\omega t) + KU_{\rm dc} + u_{\rm comm} \\ u_N = +U_O \sin(\omega t) + (1-K)U_{\rm dc} + u_{\rm comm} \\ i_P = I_{\rm cir} + I_O \sin(\omega t + \varphi) \\ i_N = I_{\rm cir} \end{cases}. \quad (20)$$

Neglecting $u_{\rm comm}$, i.e., the circulating current control voltage imposed on the inductor, the arm power with this control is expressed as

$$\begin{cases} P_P = KU_{\rm dc} I_{\rm cir} - \frac{U_O I_O}{2}\cos\varphi + \frac{U_O I_O}{2}\cos(2\omega t + \varphi) \\ +KU_{\rm dc} I_O \sin(\omega t + \varphi) - U_O I_{\rm cir} \sin(\omega t) \\ P_N = (1-K)U_{\rm dc} I_{\rm cir} + U_O I_{\rm cir} \sin(\omega t) \end{cases}. \quad (21)$$

It can be seen that if $I_{\rm cir}$ is utilized to charge arms, most of the power will be imposed on the lower arm, with less energy distribution on the upper arm, as its dc voltage is much higher than the upper arm. Therefore, the two arms' energy control is absolutely decoupled in a low-voltage condition.

The arms should alternate their roles during operation. In one period, the upper arm generates the required quantities for load, and the lower arm regulates its energy for capacitor voltage ripple reduction. In the subsequent period, the lower arm generates load quantities, but the upper arm regulates its energy.

This operation is depicted in Fig. 2. From 0 to 0.25 s, the upper arm generates ac current for the load, and its capacitor voltage drops because of its power consumption. Meanwhile, the lower arm current is zero; thus, the lower capacitor voltage also becomes zero. At 0.25 s, the two arms alternate their modes. The current varying rates are limited in preventing the circulating current; thus, the controller is capable of tracking its reference signal, which also decreases di/dt. It is shown that the output current will not be influenced by a limiter. This is because the two arms change their current simultaneously following the same direction, but their difference remains constant. From 0.25 to 0.5 s, the lower arm generates ac current for load and the upper arm generates high dc voltage, with small dc current flowing to charge the cells. Though the charge current magnitude is small, it significantly changes the capacitor voltage. It is also shown that the output line voltage (average model) is sinusoidal though the arm voltage changes dramatically; thus, the output current keeps sinusoidal. The dc side current is small except alternating transiences.

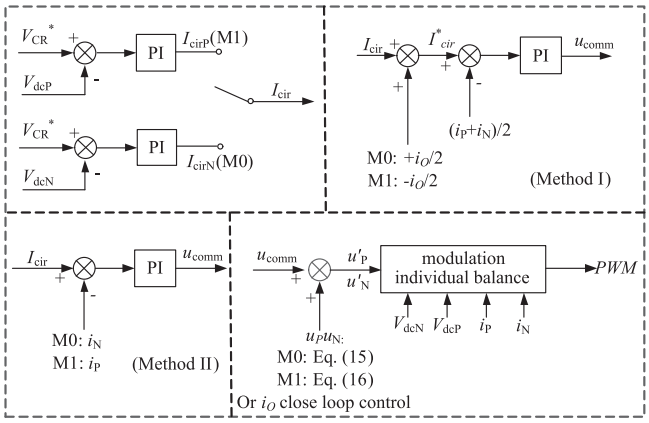

Fig. 3. Controller structure for asymmetric operation.

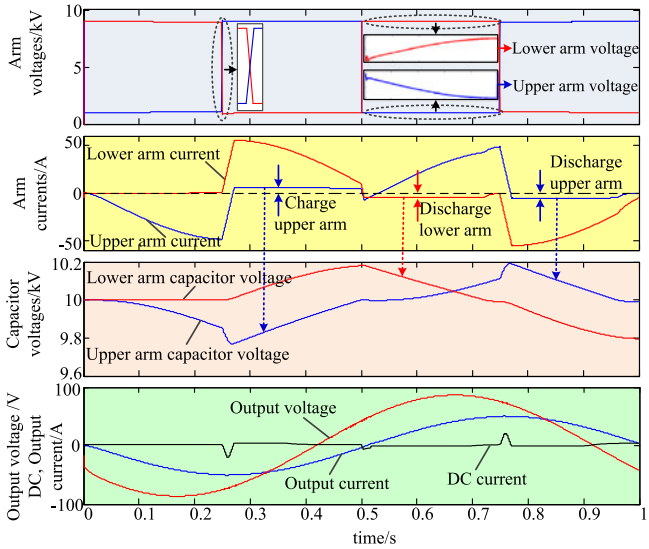

Fig. 2. Asymmetric mode operation.

C. Controller design

The controller is shown in Fig. 3. "M0" refers to the mode that the upper arm generates the converter output quantities and "M1" refers to the mode that the lower arm generates the output. To avoid the controller integral windup, two separate PI controllers are employed and work independently for capacitor energy adjustment. The upper arm capacitor voltage $V_{\mathrm{dc}P}$ and lower arm capacitor voltage $V_{\mathrm{dc}N}$ are compared with the reference voltage V^*_{CR}, and the difference is the input of the proportional-integral (PI) controller. The PI output is selected as the charging current I_{cir} for different modes. Irrespective of whether their outputs are selected or not, these two PI controllers are continuously calculated, reflecting the actual real-time power requirement for arms.

One PI controller is selected for the circulating current control. To obtain a fast response, the proportional gain is much greater than the integral part, and the latter is utilized to eliminate the capacitor voltage steady-state error in periods of output signals. Considering the output power consumption as a disturbance, and the fact that the circulating current control loop is much faster than the capacitor voltage control loop, when the arm is active for energy regulation, the capacitor voltage controller is simplified as

$$\begin{cases} I_{\mathrm{cir}} = (V^*_{\mathrm{CR}} - V_{\mathrm{dc}}) \quad (K_{\mathrm{pV}} + K_{\mathrm{iV}}/s) \\ V_{\mathrm{dc}} \approx \frac{1}{sC_a} I_{\mathrm{cir}} \end{cases} \tag{22}$$

where the $C_a = C/N$ is the equivalent capacitor value of arms. From this equation, we have

$$V_{\mathrm{dc}} = \frac{(K_p s + K_i)}{C_a s^2 + K_p s + K_i} V^*_{\mathrm{CR}}. \tag{23}$$

With a small K_i, the characteristic polynomial of this equation is $s + K_p/C_a$, where K_p can be set as $K_p = \omega_v C_a$, ω_v is the bandwidth of the capacitor voltage control with value $\omega_v = 2\pi \times F_a$, and F_a is larger than the alternating frequency, for example, $F_a \geq 4f_O$ in Fig. 2.

Using Method I, I_{cir} plus output current ($+i_O/2$ or $-i_O/2$) is the circulating current reference I^*_{cir}. After closed-loop control, the common mode voltage u_{comm} for circulating current tracking is obtained. Using Method II, the arm current (i_P or i_N) is directly driven to the charging current I_{cir} through circulating current control.

At last, calculating the upper and lower arm voltage from (15) or (16) according to different modes, and considering the circulating current control voltage u_{comm}, the arm voltage reference values u'_p and u'_N for M0 and M1 modes are achieved and rewritten as follows:

$$\begin{cases} u'_P &= -U_O \sin(\omega t) + u_{\mathrm{comm}} + KU_{\mathrm{dc}} \\ u'_N &= +U_O \sin(\omega t) + u_{\mathrm{comm}} + U_O\,(1-K)\,U_{\mathrm{dc}} \end{cases} \tag{24}$$

$$\begin{cases} u'_P &= -U_O \sin(\omega t) + u_{\mathrm{comm}} + U_O\,(1-K)\,U_{\mathrm{dc}} \\ u'_N &= +U_O \sin(\omega t) + u_{\mathrm{comm}} + KU_{\mathrm{dc}}. \end{cases} \tag{25}$$

IV. Experimental Results and Discussion

A. Platform

A verification was performed using a two-phase MMC platform with three SMs per arm, as shown in Fig. 4. A resistor–inductor load was connected to the terminals of these two phases. The central control algorithms were implemented on TMS320F28335 DSP plus EP3C25Q240C8 FPGA. The DSP realizes the circulating current and output current related close loop control and the FPGA realizes the capacitor voltage measurement, modulation, individual capacitor voltage control, and communication with SMs via optical fibers.

System parameters are listed in Table I. The load resistor is adjusted to maintain the converter current amplitude constant with variation in converter output voltage for testing.

B. Experimental Waveform With Proposed Control

Fig. 5 shows the experimental results of the proposed method operating at 1 Hz. It is shown that the upper and lower arms alternate their operating modes four times in each period.

Fig. 4. Experimental platform. (a) Front side. (b) Back side.

TABLE I
PARAMETERS OF THE EXPERIMENTAL SETUP

Parameters	Value
Number of SMs per arm, N	3
SM capacitance, C	1867 μ F
Phase-arm inductors, L	5 mH
Rated power, P_{NO}	1.25 kW
dc-link voltage, U_{dc}	550 V
SM switching frequency, f_s	3 kHz
Output voltage frequency, f_0	1–15 Hz
Output voltage amplitude, U_O	10–150 V
Load current amplitude, I_O	3 A, 5 A
Load inductor, L_O	6 mH

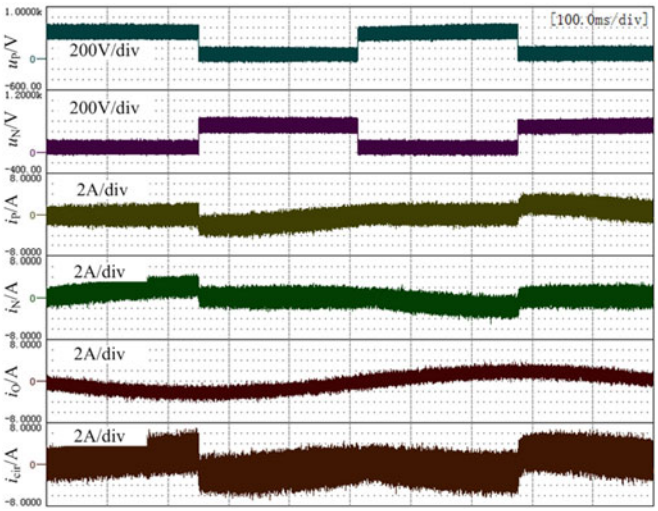

Fig. 5. Experimental waveform of arm quantities.

During the first mode, the upper arm voltage contains a high dc component approximately like the dc link voltage, but the arm current is close to zero. The lower arm voltage has a small dc quantity, but it generates ac current contributing to the output. In the following mode, the upper and lower arms exchange their operation mode, which is the same as shown in Fig. 2 (simulation results). The output and the circulating currents are derived from a math function in an oscilloscope, and are, respectively, the difference and sum of the upper arm and lower arm currents.

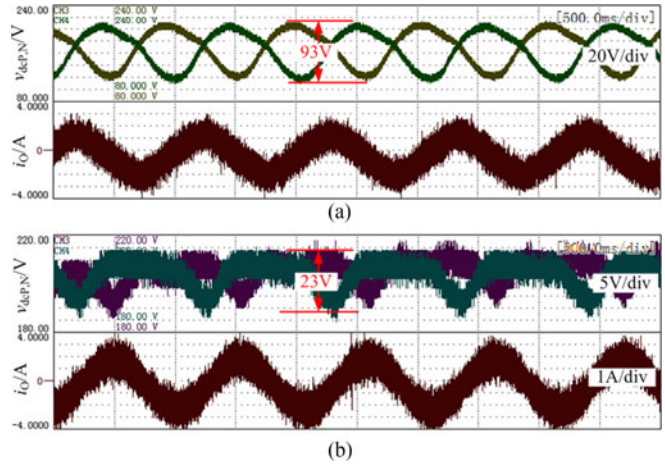

Fig. 6. Capacitor voltage ripple comparison with conventional symmetric control and the proposed asymmetric control.

A comparison of capacitor voltage ripples between a conventional and the proposed control at 1 Hz is shown in Fig. 6. The converter voltage amplitude is 15 V, and the output-current amplitude is 3 A. It is shown that the capacitor voltage with the proposed control has a ripple amplitude of 23 V, much lower than the conventional symmetric mode control, which is 93 V.

C. Capacitor Voltage Ripple Amplitude and Alternating Frequency

Considering the condition that the alternating frequency is low, such as four times in one period, the circulating current is utilized only for compensating the power phase; the phase power P_P plus P_N should be kept equivalent during one fundamental period so that the circulating current can be estimated as

$$I_{\mathrm{cir}} = \frac{U_O I_O \cos\varphi}{2U_{\mathrm{dc}}}. \tag{26}$$

From the power expression in asymmetric mode (21), the integral time is one-fourth of the fundamental period $[1/(4f_0)]$, given as

$$\begin{aligned}\tilde{V}_{\mathrm{dc}P} = \frac{1}{CV_{C0}}\Bigg[&\left(KU_{\mathrm{dc}}I_{\mathrm{cir}} - \frac{U_O I_O}{2}\cos\varphi\right)\frac{1}{4f_0} \\ &+ \frac{U_O I_O}{4\omega}\sin(2\omega t+\varphi) - \frac{KU_{\mathrm{dc}}I_O}{\omega}\cos(\omega t+\varphi) \\ &+ \frac{U_O I_{\mathrm{cir}}}{\omega}\cos(\omega t)\Bigg].\end{aligned} \tag{27}$$

It is worth noticing that $KU_{\mathrm{dc}}{=}U_O$, and I_{cir} is small at a low frequency, so this equation shows that the capacitor voltage ripple amplitude is related only to the converter output voltage and current (or output power).

A comparative result at a high power is shown in Fig. 7. The output voltage and current amplitudes $(U_O,\ I_O)$ are 30 V and 5 A, respectively; therefore, the converter output power is 3.33 times greater than that of the condition in Fig. 6. The capacitor

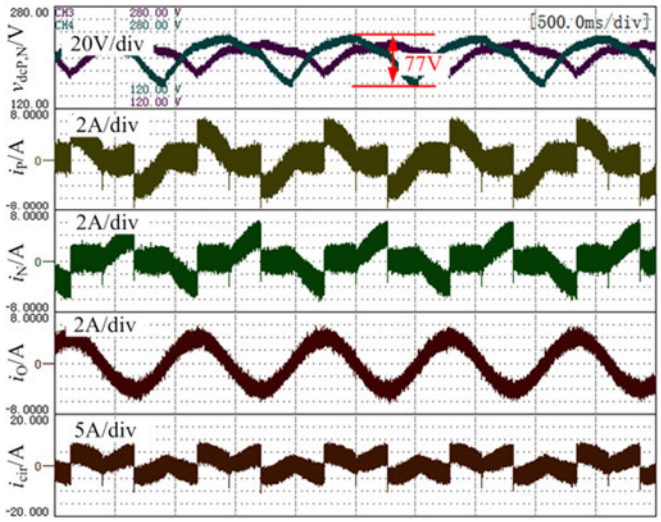

Fig. 7. Capacitor voltage ripple as the alternating frequency is $4f_O$.

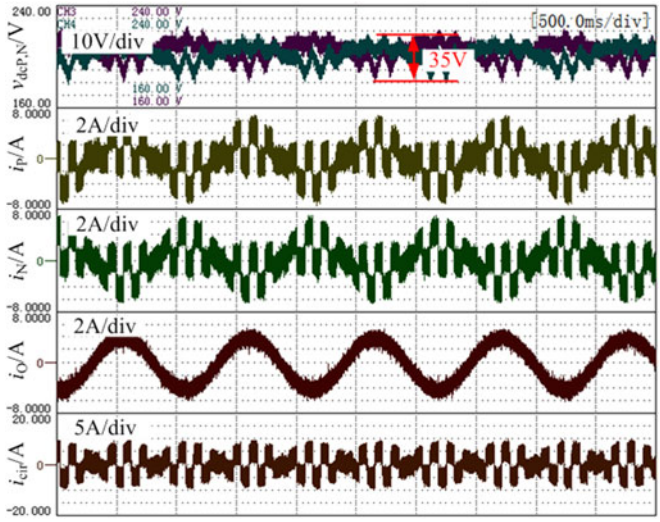

Fig. 8. Capacitor voltage ripple as the alternating frequency is $16f_O$.

voltage ripple amplitude ratio is 77 V/23 V = 3.34, which is similar to the power ratio and verifies the relationship between converter power and capacitor voltage ripples.

However, since the arm energy control is decoupled at a low-voltage condition, the capacitor voltage ripple can be further attenuated by increasing the alternating frequency. This can be helpful during motor zero frequency operation, in which the controller can adjust arm energy very effectively. Results in Fig. 8 show operations when the alternating frequency is 16 f_O: The rapid alternating operation will decrease the capacitor voltage ripple, obviously. The reduction will be influenced by the circulating current tracking capability and control loop design. Actually, if the alternating frequency is high, this control acts as a high-frequency injection method.

D. Effectiveness and Limitation in Full Speed Range

There is a need to study the performance of the proposed method at full speed. Considering the motor V/f control, from

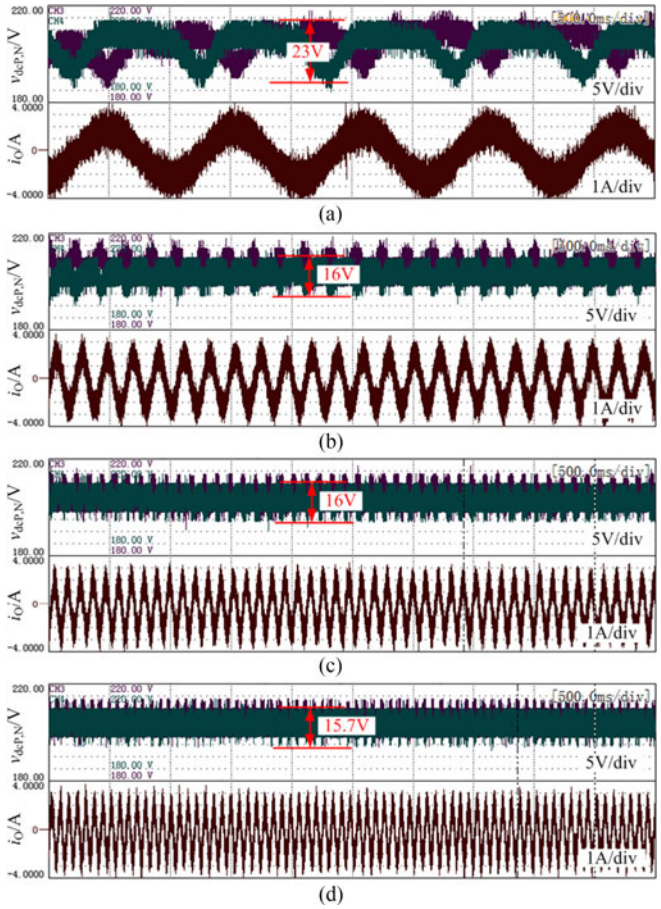

Fig. 9. Capacitor voltage ripple at a different frequency f_O and output voltage U_O.

(12), (17), (26), and (27), and noticing that $\omega_0 = 2\pi f_0$, $U_{\rm dc} = 2U_M$, the arm capacitor voltage ripple with a low-alternating frequency ($4f_0$) is

$$\tilde{V}_{{\rm dc}P} = \frac{f_O I_O \cos\varphi}{8 f_M}\cos(\omega_0 t) - \frac{I_O}{2}\cos(\omega_0 t + \varphi) + \frac{U_M I_O}{C V_{C0} f_M \pi}\left[\frac{\pi}{4}\left(\frac{f_0\cos\varphi}{4f_M} - \frac{\cos\varphi}{2}\right) + \frac{\sin(2\omega_0 t + \varphi)}{8}\right] \tag{28}$$

which indicates that if f_0 is small, the first term is negligible and the capacitor ripple, being only proportional to the output current amplitude, is constant. When f_0 increases, the ripple will increase slightly, which is evident from experimental results, as depicted in Fig. 9, showing the capacitor voltage ripples at different frequencies and converter voltages. The ratio of voltage to frequency equals to 10, which simulates the motor drive V/f control. Because of the deadtime impact at low modulation indices, in order to obtain the same magnitude of current, the voltage at the 1 Hz condition has to be 15 V. The converter current magnitude remains the same at different operating points by adjusting the load resistor. It is shown that ripple amplitudes approximately remain the same when the operation frequency varies.

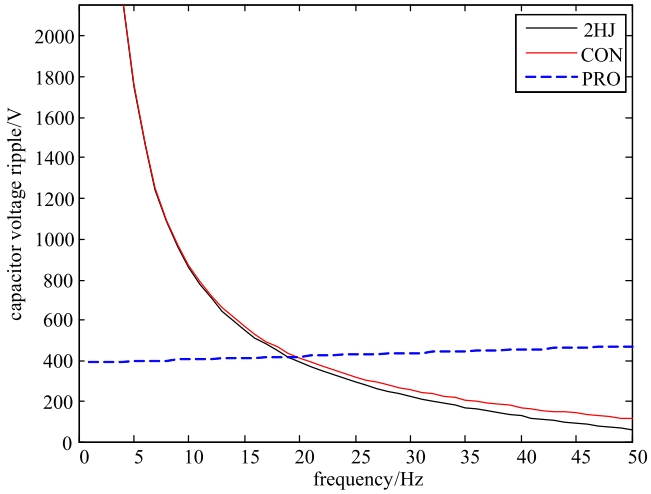

Fig. 10. Capacitor voltage ripple with different controls.

TABLE II
PARAMETERS OF THE SIMULATION SYSTEM

Parameters	Value
Number of SMs per arm, N	3
SM switching frequency, f_s	3 kHz
SM capacitance, C	1500 μ F
Phase-arm Inductors, L	10 mH
dc-link voltage, U_{dc}	9 kV
Output voltage frequency, f_0	1–50 Hz
Output voltage amplitude, U_O	90 V–4.5 kV
Load current amplitude, I_O	50 A
Power factor angle φ	$[0, \pi/2]$

V. DISCUSSION

A. Limitations

The control performance of the capacitor ripple with different controls for a motor drive in a full speed range is compared and shown in Fig. 10. The power of conventional control (CON), second harmonic injection method (2HJ), and the proposed method (PRO) is calculated through (11) and (21), and then the capacitor voltage is obtained [14]. The parameters are listed in Table II. Change f_0 from 1 to 50 Hz and the corresponding U_O in terms of (12), and measure the ripple amplitude at each point. The results shows that the symmetric mode control (CON and 2HJ) will result in a significant capacitor voltage ripple in a low speed range, which is inversely proportional to frequency. The proposed asymmetric mode control has excellent performance at low speed, and the ripple amplitude varies slightly in a full speed range, which is in accordance with Fig. 9. However, the symmetric control has better performance when the frequency is higher than 20 Hz. This means that the proposed asymmetric mode control is suitable for operation at a frequency below 20 Hz (0%–40% speed range), and the control needs to switch to a conventional symmetric mode in a middle or high-speed range. However, as mentioned before, increasing the alternating operation frequency can enhance the ripple suppression effect of the proposed method.

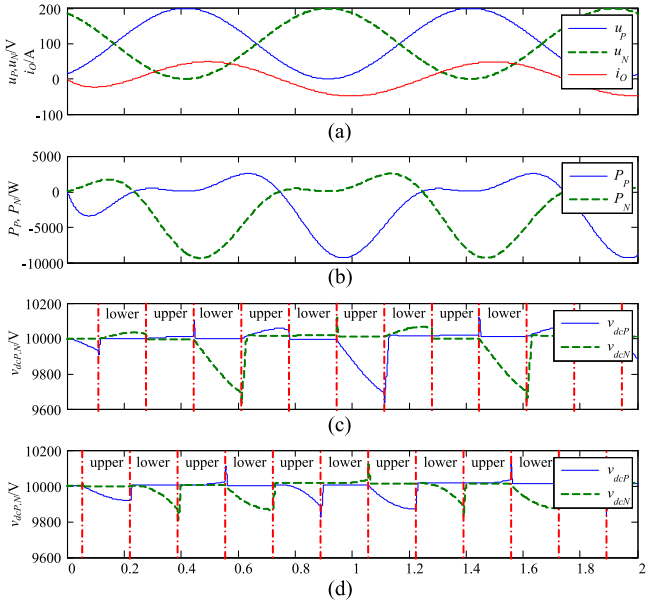

Fig. 11. Capacitor voltage ripple with different alternating point selecting schemes.

B. Alternating Point Optimization for Three-Phase System

The alternating point will influence the capacitor voltage ripple amplitude. This can be seen from (11). The simulation results with the parameters are shown in Table II. The arm voltages have a dc shift equal to KU_{dc}, which maintains the voltage magnitudes at a value greater than zero. If the arms generate the output quantities continuously, the corresponding instantaneous power is displayed in Fig. 11(b). As shown in Fig. 11(c) and (d), the capacitor voltage ripples are affected by large variations with different alternating points selecting schemes. The ripple in (d) has a smaller amplitude, and the reason is that it chooses the arm with less power flow to generate the output quantities. For example, between 0.38 and 0.55 s, from (b), if the lower arm generates output quantities, this arm will sustain high power transfer. However, if the upper arm generates output quantities, the power flow has a smaller magnitude. Compared with (c), the alternating point selecting scheme in (d) avoids the maximum zone of power to achieve a smaller capacitor voltage ripple.

Ignoring the circulating components and rewriting the arm power (19), if the upper arm generates output, its instantaneous power has the form

$$P_P = U_O I_O \left(1 - \sin\left(\omega t\right)\right) \sin\left(\omega t + \varphi\right). \tag{29}$$

Similarly, if the lower arm generates output, the power becomes

$$P_N = U_O I_O \left(1 + \sin\left(\omega t\right)\right) \left(-\sin\left(\omega t + \varphi\right)\right). \tag{30}$$

From (29) and (30), it is easy to deduct that, if the upper arm has its maximum at the point of ωt_0, the lower arm will get its maximum at the point of $(\omega t_0 + \pi)$.

The relationship between the maximum point and different power factors is shown in Fig. 12, and the angle of horizontal axis is the voltage phase angle. The maximum point is $\omega t = \pi/2$

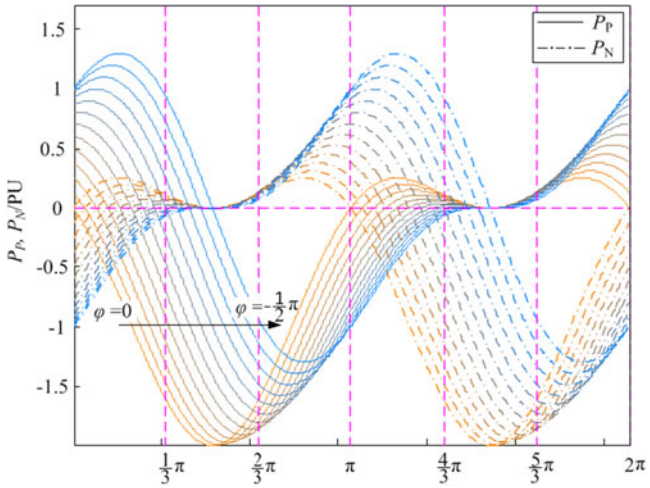

Fig. 12. Power maximum points with different power factor angles.

when the power factor angle $\varphi = 0$, and it is $\omega t = 5\pi/6$ when the power factor angle $\varphi = -\pi/2$. The accurate points can be achieved through an offline calculation, and the approximate value is given as

$$\omega t^* = -\left(\frac{\pi}{2} + \frac{\varphi}{\pi/2}\left(\frac{5\pi}{6} - \frac{\pi}{2}\right)\right) = -\left(\frac{\pi}{2} + \frac{2\varphi}{3}\right). \quad (31)$$

It should be noted that the maximum points of instantaneous power alternately appear with an equal phase shift in three-phase systems such as motor drives, as shown in Fig. 13(c). Assuming the upper arm of a-phase has maximum power at ωt^* and the upper arm of c-phase has maximum power at $(\omega t^* + 2\pi/3)$, and the lower arm of c-phase will has its maximum power at $(\omega t^* + 2\pi/3 + \pi)$, or $(\omega t^* - \pi/3)$. With similar analysis, the three phases' power will achieve maximum after a phase angle of $\pi/3$, and the upper arm and lower arm get maximum alternately, as shown in Fig. 13(c). Therefore, the optimized alternating strategy is to divide one period into six sectors, each from $(\omega t - \pi/6)$ to $(\omega_0 t + \pi/6)$, where $\omega_0 t$ is the point where the arm power achieves maximum, and then select the arm with less power as the working arm generating output quantities so as to avoid high-power flows in arms. With this alternating point optimization method, the arm capacitor voltage ripple is about 300 V, which is smaller than the results in Fig. 10 at 1 Hz. The dc current is shown in Fig. 13(b), which contains a small magnitude of harmonics. The arm producing voltage and output line voltage are shown in Fig. 13(e). It can be seen that the arms alternately generate a high DC voltage, and the sum of the two voltages is approximately equal to the dc-link voltage.

The alternating point optimization control is depicted in Fig. 14. The motor control is always implemented in the d–q vector frame; thus, the angles of voltage and current phasors are easy to obtain by the "atan" function, and their difference, power factor angle φ, is used to calculate the maximum power point. After the maximum point θ_0 has been achieved, the sectors and their corresponding working modes are determined.

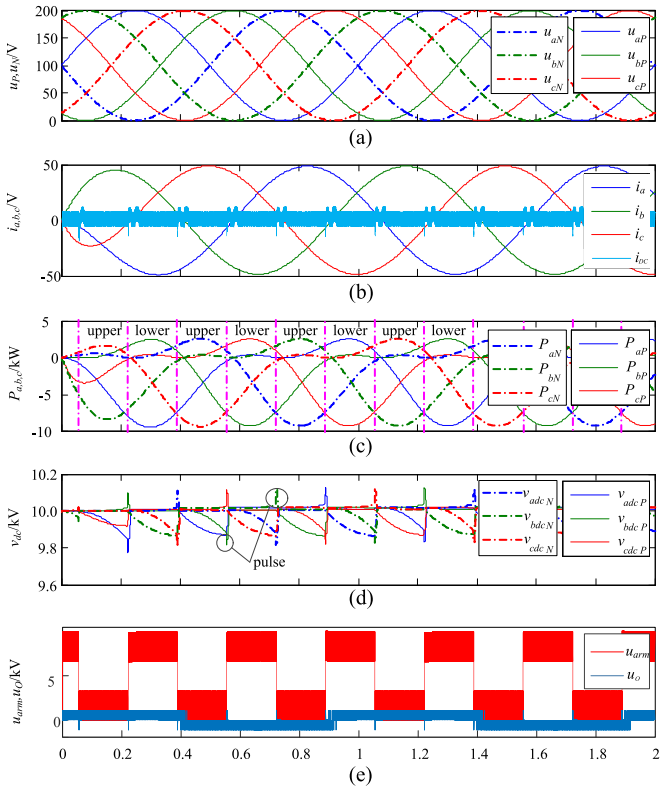

Fig. 13. Optimized alternating operation in a three-phase system.

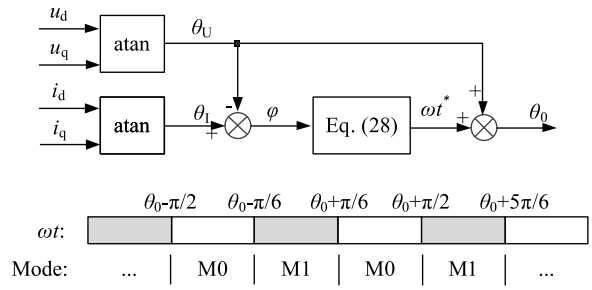

Fig. 14. Working mode after alternating point optimization.

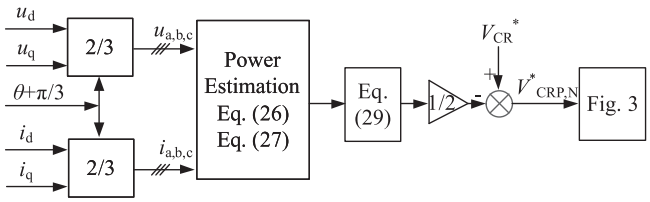

Fig. 15. Power estimation for capacitor voltage reference value optimization.

It should also be pointed out that a much higher alternating frequency can also be applied in a three-phase system, but the optimized effect for the capacitor voltage ripple reduction will not be kept, and the control becomes another form of high-frequency injection method.

C. Energy Prediction Control

The circulating current will change greatly at the alternating point, and one rate limiter is utilized to reduce di/dt. In Fig. 13,

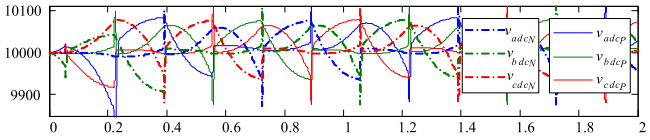

Fig. 16. Capacitor voltage with alternating point and energy prediction based optimization control.

the transient process lasts about 2 ms. This process does not influence the output current as mentioned before; however, it influences the power decoupling control between two arms. The pulse in capacitor voltage ripples, as shown in Fig. 13(d), is just from the transient process of alternating operation.

From Fig. 13(d), it can be found that if the capacitor voltage of the arm that does not generate the output quantities regulates its voltage at a value higher than the rating value, then its voltage will not fall down so much in the next sector. With the help of (29) and (30), or the more detailed model in (21), the capacitor voltage ripple in the next sector can be easily estimated as

$$\tilde{V}_{\mathrm{dc}P} = \frac{1}{CV_{C0}} \int_{\omega_0 t-\frac{\pi}{6}}^{\omega_0 t+\frac{\pi}{6}} P_P \, dt. \tag{32}$$

The energy prediction control is shown in Fig. 15. The voltage and current in the next sector are calculated by 2/3 transformation, so the power and the capacitor voltage ripple can be estimated through (29), (30), and (32). The capacitor voltage reference value V_{CR}^{*} minus half of the estimated capacitor voltage ripple is the new reference value for capacitor voltage control.

The capacitor voltage with the optimized control is displayed in Fig. 16: It is not regulated at the rating value when this arm does not generate output quantities, which helps to reduce the voltage variation in the next-step mode. Compared with Fig. 13(d), the capacitor voltage ripple with this control is further reduced to 225 V.

D. Comparison With Other Controls

There are several methods concerning reducing MMCs' capacitor voltage with low frequency operation capability. Though they share some characteristics such as employing zero sequence voltage, they regulate the arm charging/discharging processes by different measures. As mentioned above, with the proposed method, one arm is shaped to have a dc-link voltage but none of the output currents, thus decoupling the arm energy control; therefore, the arm energies are regulated by two independent PI controllers directly. While using a high-frequency injection method, such as in [18]–[21], common mode (zero sequence) voltage is injected at a neutral point, incorporating the same frequency components in the circulating current, resulting in active power to exchange between the upper and lower arm energy. Because of the significant magnitude of power imbalance, as presented in (13), the injected circulating current must be large enough to balance the arm energy. The discontinuous modulation-based method [27], [28], in which one arm is clamped to upper or lower terminals and another arm supports dc-link voltage, reduces the capacitor voltage ripples (like the

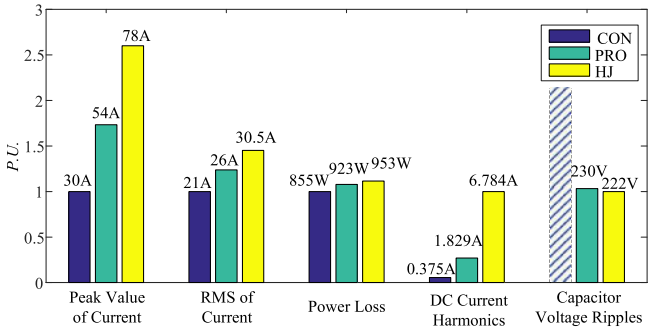

Fig. 17. Performance comparison among different controls.

proposed method does), but the arm current is not optimized as in the proposed method to achieve energy decoupling, and its energy balance is the same as conventional control [14], [17]; thus, the circulating (charging/discharging) current expression is different from that derived in this paper. The switching cycle regulating based method [29] adjusts the upper and lower arm current at a certain value according to the arm voltage to minimize the capacitor voltage ripples. Apparently, it is similar to the proposed method, but with the following differences:

1) the current regulation is completed in specific transient switching states, and the arm inductance must be small enough to achieve this goal;
2) the current and capacitor voltage are open-loop controlled without accounting for any accumulative error influence;
3) the zero sequence voltage is not utilized explicitly and the results are given only under the condition that each arm contains one or two cells.

A comparison with the popular high-frequency injection method, regarding current stress, power loss, and dc current harmonics, is shown in Fig. 17.

1) The square common mode voltage and sinusoidal circulating current (50 Hz) are injected for the HJ method. The injected voltage has the maximal value limited only by modulation index.
2) The HJ method [21] and the proposed method have the same working conditions as listed in Table II (on 1 Hz), and they have the same level of capacitor voltage ripples. The CON [14] is applied as a reference, but its capacitor voltage is set as a constant during simulation to ensure that it can work on such low frequency. So, the capacitor voltage ripple magnitude is not shown in Fig. 17.
3) The current stress is illustrated by the current peak and root-mean-square (RMS) values.
4) The power loss, including switching and conducting losses, is obtained by an average value of energy accumulating from simulation data in 2 s.
5) The dc current harmonics results are from the FFT tools in Simulink.

It is shown that the high-frequency injection and the proposed method have both a larger peak current than conventional control. The high-frequency injection method has a maximal peak current to attenuate its capacitor voltage ripples. This means that the proposed method has a higher energy balance

efficiency than the high-frequency injection method. The RMS values and power loss have an accordant phenomenon with the peak current.

The high-frequency injection method and the proposed method both have relatively small dc current harmonics in a three-phase system in contrast with the magnitude of arm current. However, the HJ method has greater ones because it needs a higher magnitude of circulating current to balance the huge power difference caused by $U_{\rm dc}$ and I_O, and the control error and slight imbalance generate high-frequency harmonics. On the other hand, the proposed method needs only a small magnitude of circulating current (or energy pulsation) to compensate for the arm power caused by U_O and I_O, as shown in (19), and the dc harmonics can be seen in Fig. 13(b).

Because of its limitation of the energy balance effect, compared with the proposed method, the HJ method needs a larger circulating current to attenuate capacitor voltage ripples, but the higher the circulating current, the higher the power loss, and the link inductance voltage will increase consequently, which shrinks the linear modulation range. Therefore, the HJ method requires more tradeoff consideration. However, it should be pointed out that the square circulating current will enhance the energy balance performance in the HJ method, but the current control will become complex.

VI. Conclusion

In an MMC with conventional symmetric energy control, upper and lower arms are coupled, resulting in a difficult arm voltage balance. This paper overcomes this problem by proposing a novel asymmetric operation control of MMC enhancing low-frequency and low-voltage operations, which is especially useful in low-speed motor drive applications. The proposed control strategy has been verified by simulation and experimental results. The main advantage is that arm energy fluctuations at low speed are majorly correlated with the converter output power, namely u_O and i_O, and are not significantly influenced by the dc-link voltage . The proposed method is suitable for high-power motor drives operating below 20 Hz, resulting in the voltage ripple remaining almost constant, especially in the startup process. However, in some special cases, the motor may require a high driving voltage (even half of the ratings) at a low frequency. The proposed method is not suitable in this situation, which will be studied in the future.

References

[1] S. Kouro *et al.* "Recent advances and industrial applications of multilevel converters," *IEEE Trans. Ind. Electron.*, vol. 57, no. 8, pp. 2553–2580, Aug. 2010.

[2] H. Akagi, "Classification, terminology, and application of the modular multilevel cascade converter (MMCC)," *IEEE Trans. Power Electron.*, vol. 26, no. 11, pp. 3119–3130, Nov. 2011.

[3] S. Debnath, J. Qin, B. Bahrani, M. Saeedifard, and P. Barbosa, "Operation, control, applications of the modular multilevel converter: A review," *IEEE Trans. Power Electron.*, vol. 30, no. 1, pp. 37–53, Jan. 2015.

[4] M. Saeedifard and R. Iravani, "Dynamic performance of a modular multilevel back-to-back HVDC system," *IEEE Trans. Power Del.*, vol. 25, no. 4, pp. 2903–2912, Oct. 2010.

[5] M. Guan and Z. Xu, "Modeling and control of a modular multilevel cconverter-based HVDC system under unbalanced grid conditions," *IEEE Trans. Power Electron.*, vol. 27, no. 12, pp. 4858–4867, Dec. 2012.

[6] A. Hassanpoor, A. Roostaei, S. Norrga, and M. Lindgren, "Optimization-based cell selection method for grid-connected modular multilevel converters," *IEEE Trans. Power Electron.*, vol. 31, no. 4, pp. 2780–2790, Apr. 2016.

[7] J. Peralta, H. Saad, S. Dennetiere, J. Mahseredjian, and S. Nguefeu, "Detailed and averaged models for a 401-level MMC– HVDC system," *IEEE Trans. Power Del.*, vol. 27, no. 3, pp. 1501–1508, Jul. 2012.

[8] I. A. Gowaid, G. P. Adam, A. M. Massoud, S. Ahmed, D. Holliday, and B. W. Williams, "Quasi two-level operation of modular multilevel converter for use in a high-power DC transformer with DC fault isolation capability," *IEEE Trans. Power Electron.*, vol. 30, no. 1, pp. 108-123, Jan. 2015.

[9] T. Luth, M. M. C. Merlin, T. C. Green, F. Hassan, and C. D. Barker, "High-frequency operation of a DC/AC/DC system for HVDC applications," *IEEE Trans. Power Electron.*, vol. 29, no. 8, pp. 4107–4115, Aug. 2014.

[10] G. J. Kish, M. Ranjram, and P. W. Lehn, "A modular multilevel DC/DC converter with fault blocking capability for HVDC interconnects," *IEEE Trans. Power Electron.*, vol. 30, no. 1, pp. 148–162, Jan. 2015.

[11] C. Cecati, F. Ciancetta, and P. Siano, "A multilevel inverter for photovoltaic systems with fuzzy logic control," *IEEE Trans. Ind. Electron.*, vol. 57, no. 12, pp. 4115–4125, Dec. 2010.

[12] J. Mei, B. Xiao, K. Shen, L. M. Tolbert, and J. Y. Zheng, "Modular multilevel inverter with new modulation method and its application to photovoltaic grid-connected generator," *IEEE Trans. Power Electron.*, vol. 28, no. 11, pp. 5063–5073, Nov. 2013.

[13] A. Antonopoulos *et al.*, "Modular multilevel converter ac motor drives with constant torque from zero to nominal speed," *IEEE Trans. Ind. Appl.*, vol. 50, no. 3, pp. 1982–1993, May/Jun. 2014.

[14] M. Hagiwara, K. Nishimura, and H. Akagi, "A medium-voltage motor drive with a modular multilevel PWM inverter," *IEEE Trans. Power Electron.*, vol. 25, no. 7, pp. 1786–1799, Jul. 2010.

[15] M. Vasiladiotis, N. Cherix, and A. Rufer, "Accurate capacitor voltage ripple estimation and current control considerations for grid-connected modular multilevel converters," *IEEE Trans. Power Electron.*, vol. 29, no. 9, pp. 4568–4579, Sep. 2014.

[16] R. Picas, J. Pou, S. Ceballos, J. Zaragoza, G. Konstantinou, and V. G. Agelidis, "Optimal injection of harmonics in circulating currents of modular multilevel converters for capacitor voltage ripple minimization," in *IEEE ECCE Asia, 2013*, pp. 318–324.

[17] J. Pou, S. Ceballos, G. Konstantinou, V. G. Agelidis, R. Picas, and J. Zaragoza, "Circulating current injection methods based on instantaneous information for the modular multilevel converter," *IEEE Trans. Ind. Electron.*, vol. 62, no. 2, pp. 777–788, Feb., 2015.

[18] M. Hagiwara, I. Hasegawa, and H. Akagi, "Start-up and low-speed operation of an electric motor driven by a modular multilevel cascade inverter," *IEEE Trans. Ind. Appl.*, vol. 49, no. 4, pp. 1556–1565, Jul./Aug. 2013.

[19] S. Debnath, J. Qin, and M. Saeedifard, "Control and stability analysis of modular multilevel converter under low-frequency Operation," *IEEE Trans. Ind. Electron.*, vol. 62, no. 9, pp. 5329–5339, Sep. 2015.

[20] J. Kolb, F. Kammerer, M. Gommeringer, and M. Braun, "Cascaded control system of the modular multilevel converter for feeding variable-speed drives," *IEEE Trans. Power Electron.*, vol. 30, no. 1, pp. 349–357, Jan. 2015.

[21] J. J. Jung, H. J. Lee, and S. K. Sul, "Control strategy for improved dynamic performance of variable-speed drives with the modular multilevel converter," *IEEE J. Emerg. Sel. Topics Power Electron.*, vol. 3, no. 2, pp. 371–380, Jun. 2015.

[22] K. Wang, Y. Li, Z. Zheng, and L. Xu, "Voltage balancing and fluctuation suppression methods of floating capacitors in a new modular multilevel converter," *IEEE Trans. Ind. Electron.*, vol. 60, no. 5, pp. 1943–1954, May 2013.

[23] L. He, K. Zhang, J. Xiong, S. Fan, and Y. Xue, "Low-frequency ripple suppression for medium-voltage dives using modular multilevel converter with full-bridge submodules," *IEEE J. Emerg. Sel. Topics Power Electron.*, vol. 4, no. 2, pp. 657–667, Jun. 2016.

[24] B. Li, Y. Zhang, G. Wang, W. Sun, D. Xu, and W. Wang, "A modified modular multilevel converter with reduced capacitor voltage fluctuation," *IEEE Trans. Ind. Electron.*, vol. 62, no. 10, pp. 6108–6119, Oct. 2015.

[25] W. Kawamura, K. Chen, M. Hagiwara, and H. Akagi, "A low-speed, high-torque motor drive using the modular multilevel cascade converter based on triple-star bridge cells (MMCC-TSBC)," in *Proc. IEEE Energy Convers. Congr. Expo.*, Nov. 11, 2014, pp. 1631–1638.

[26] L. Baruschka and A. Mertens, "A new three-phase ac/ac modular multilevel converter with six branches in hexagonal configuration," *IEEE Trans. Ind. Appl.*, vol. 49, no. 3, pp. 1400–1410, May/Jun. 2013.

[27] R. Picas, S. Ceballos, J. Pou, J. Zaragoza, G. Konstantinou, and V. G. Agelidis, "Improving capacitor voltage ripples and power losses of modular multilevel converters through discontinuous modulation," in *Proc. 39th Annu. Conf. IEEE Ind. Electron. Soc.*, 2013, pp. 6233–6238.
[28] R. Picas, S. Ceballos, J. Pou, J. Zaragoza, G. Konstantinou, and V. G. Agelidis, "Closed-loop discontinuous modulation technique for capacitor voltage ripples and switching losses reduction in modular multilevel converters," *IEEE Trans. Power Electron.*, vol. 30, no. 9, pp. 4714–4725, Sep. 2015.
[29] J. Wang, R. Burgos, and D. Boroyevich, "Switching-cycle state-space modeling and control of the modular multilevel converter," *IEEE J. Emerg. Sel. Topics Power Electron.*, vol. 2, no. 4, pp. 1159–1170, Dec. 2014.

Rongfeng Yang received the B.S., master's, and doctoral degrees, all in engineering physics, from Tsinghua University, Beijing, China, in 2001, 2003, and 2006, respectively.

In 2006, he joined as a Lecturer in the Department of Electrical Engineering, Harbin Institute of Technology, Harbin, Heilongjiang, China,, where he finished his postdoctoral work. From 2014 to 2015, he was a Visiting Scholar in the Center for Power Electronics Systems, Virginia Tech, Blacksburg, VA, USA. In 2016, he joined the School of Marine Engineering, Jimei University, Xiamen, China. His research interests include sensorless induction motors control and high power medium voltage applications.

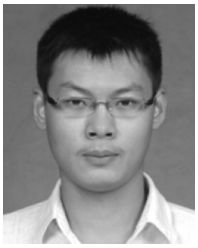

Binbin Li (S'15) was born, in 1989. He received the B.S. and M.S. degrees in electrical engineering, in 2010 and 2012, respectively, from the Harbin Institute of Technology, Harbin, China, where he is currently working toward the Ph.D. degree.

From July to November 2012, he was with the Silergy Corporation, Hangzhou, China. Currently he is a Visiting Researcher in the Department of Electronic and Electrical Engineering, University of Strathclyde, Glasgow, U.K. His research interests include high-power electronics, multilevel converters, control algorithms, and PWM techniques.

Gaolin Wang (M' 13) received the B.S., M.S., and Ph.D. degrees in electrical engineering from the Harbin Institute of Technology, Harbin, China, in 2002, 2004, and 2008 respectively.

In 2009, he joined as a Lecturer in the Department of Electrical Engineering, Harbin Institute of Technology, where he has been a Full Professor of electrical engineering since 2014. From 2009 to 2012, he was a Postdoctoral Fellow in the Shanghai Step Electric Corporation, Shanghai, China, where he was involved in the traction machine control for direct-drive elevators. His research interests include permanent magnet synchronous motor drives, high performance direct-drive for traction system, position sensorless control of AC motors, efficiency optimization control of PMSM, and digital control of power converters.

He has authored more than 50 technical papers published in journals and conference proceedings. He is the holder of 10 Chinese patents.

Carlo Cecati (M' 90–SM' 03–F' 06) received the Dr. Ing. degree in electrotechnical engineering from the University of L'Aquila, L'Aquila, Italy, in 1983.

Since 1983, he has been a Professor of industrial electronics and drives with the University of L' Aquila, L' Aquila, Italy. Since 2015, he has also been a Qianren Talents Professor (1000 Talents Program distinguished professor) with the Harbin Institute of Technology, Harbin, China. His research interests include power electronics, distributed generation, and smart grids.

Dr. Cecati has authored more than 150 journal and conference papers. From 2013 to 2015, he was the Editor-in-Chief of the IEEE TRANSACTIONS ON INDUSTRIAL ELECTRONICS. He is a co-recipient of the 2012 and the 2013 Best Paper Awards from the IEEE TRANSACTIONS ON INDUSTRIAL INFORMATICS and of the 2012 Best Paper Award from the IEEE INDUSTRIAL ELECTRONICS MAGAZINE. He is the CTO at DigiPower srl., a University of L'Aquila spin-off.

Shaoze Zhou was born, in 1993. He received the B.S. degree in electrical engineering from Hohai University, Nanjing, China. Since 2015, he has been working toward the Ph.D. degree in the Harbin Institute of Technology, Harbin, China.

His research interests include multilevel converters, motor drives, and control algorithms.

Dianguo Xu (M'97–SM'12) received the B.S. degree in control engineering from Harbin Engineering University, Harbin, China, in 1982, and the M.S. and Ph.D. degrees in electrical engineering from the Harbin Institute of Technology (HIT), Harbin, China, in 1984 and 1989, respectively.

In 1984, he was an Assistant Professor in the Department of Electrical Engineering, HIT. Since 1994, he has been a Professor in the Department of Electrical Engineering, HIT. From 2000 to 2010, he was the Dean of the School of Electrical Engineering and Automation, HIT. He is currently the Vice-President of HIT. His research interests include renewable energy generation technology, multiterminal HVDC system based on VSC, power quality mitigation, speed sensorless vector controlled motor drives, and high-performance PMSM servo systems.

Dr. Xu has published over 600 technical papers. He is an Associate Editor of the IEEE TRANSACTIONS ON INDUSTRIAL ELECTRONICS and the IEEE JOURNAL OF EMERGING AND SELECTED TOPICS IN POWER ELECTRONICS. He is also serving as the Chairman of the IEEE Harbin Section, Director of the Lighting Power Supply Committee of CPSS, and Vice-Director of the Electric Automation Committee of CAA, Electrical Control System & Equipment Committee of CES, and Power Electronics Committee of CES.

Wanneng Yu received the M.S and Ph.D. degrees in power electronic and electrical drive from Shanghai Maritime University, Shanghai, China, in 2005 and 2010, respectively.

Since 2014, he has been a Professor in the School of Marine Engineering, Jimei University, Xiamen, China. His research interests include the shipping electric propulsion, shipping multienergy power system, and dynamic positioning system.